

# Cavity-control of bright and dark interlayer excitons in van der Waals heterostructures

Michael Förg,<sup>1</sup> Léo Colombier,<sup>1</sup> Robin K. Patel,<sup>1</sup> Jessica Lindlau,<sup>1</sup> Aditya D. Mohite,<sup>2</sup> Hisato Yamaguchi,<sup>2</sup> David Hunger,<sup>3</sup> and Alexander Högele<sup>1</sup>

<sup>1</sup>*Fakultät für Physik, Munich Quantum Center, and Center for NanoScience (CeNS), Ludwig-Maximilians-Universität München, Geschwister-Scholl-Platz 1, D-80539 München, Germany*

<sup>2</sup>*MPA-11 Materials Synthesis and Integrated Devices, Materials Physics and Applications Division, Los Alamos National Laboratory (LANL), Los Alamos, New Mexico 87545, USA*

<sup>3</sup>*Physikalisches Institut, Karlsruher Institut für Technologie, Wolfgang-Gaede-Straße 1, 76131 Karlsruhe, Germany*

(Dated: October 26, 2017)

Monolayer (ML) transition metal dichalcogenides (TMDs) integrated in optical microcavities host exciton-polaritons as a hallmark of the strong light-matter coupling regime. Analogous concepts for hybrid light-matter systems employing spatially indirect excitons with a permanent electric dipole moment in heterobilayer (HBL) crystals promise realizations of exciton-polariton gases and condensates with immanent dipolar interactions. Here, we identify optical signatures of spatially indirect momentum-bright and momentum-dark interlayer excitons in vertical MoSe<sub>2</sub>-WSe<sub>2</sub> heterostructures and implement cavity-control of both exciton manifolds. Our experiments quantify the strength of light-matter coupling for both zero and finite momentum excitons residing in Moiré superlattices of TMD HBLs and demonstrate that both exciton species are susceptible to Purcell enhancement in cavity-modified photonic environments. Our results form the basis for further developments of dipolar exciton-polariton gases and condensates in hybrid cavity – van der Waals heterostructure systems.

Semiconductor TMDs exhibit remarkable optoelectronic and valleytronic properties in the limit of direct band-gap MLs [1–4]. High oscillator strength renders the materials ideal for the studies of collective strong coupling phenomena mediated among excitons and photons by optical resonators. This limit of new bosonic eigenstates of half-matter and half-light quasiparticles known as exciton-polaritons was first observed for ML TMDs with MoS<sub>2</sub> in a planar microcavity at room temperature [5]. Subsequent studies established enhanced coupling rates for cavity-integrated WS<sub>2</sub> MLs [6]. Combinations of dielectric and metallic mirrors allowed the observation of Tamm-plasmon polaritons [7] with substantial degrees of valley polarization [8], while additional control of the TMD doping level has enabled studies of fermionic polaron-polaritons [9].

In contrast to TMD MLs, cavity-control of their heterobilayer (HBL) counterparts has been elusive despite their potential for fundamental studies of dipolar gases with intriguing polarization dynamics upon expansion [10] and condensation phenomena [11]. Composed of two dissimilar MLs in staggered band alignment [12, 13], such van der Waals heterostructures host layer-separated electron-hole pairs in response to optical excitation [14]. The spatial separation of Coulomb-correlated electrons and holes gives rise to a permanent exciton dipole moment along the stacking axis and extended lifetimes up to hundreds of ns [14–17]. While long lifetimes are beneficial in providing sufficient time for thermalization, finite exciton dipole moments underpin mutual interactions in exciton-polariton gases and condensates. To date, however, the integration of HBLs into optical cavities has been impeded by the involved fabrication method of exfoliation-stacking which requires careful alignment of both MLs along the crystallographic axes to reduce momentum mismatch between electrons and holes residing in dissimilar layers.

As opposed to exfoliation-stacking, chemical vapor deposition (CVD) realizes inherently aligned TMD heterostructures with atomically sharp interfaces both in lateral and vertical geometries [18, 19]. Such CVD-grown vertical MoSe<sub>2</sub>-WSe<sub>2</sub> heterostructures were used in our experiments to demonstrate cavity-control of interlayer excitons for the first time. To this end we employed a tunable open-access cavity with one curved fiber-based mirror and one planar mirror with extended heterostructure flakes on top (see Supplementary Information for details on sample fabrication). The configuration of controlled intermirror spacing and lateral scanning capabilities with proven potential in the studies of other low-dimensional condensed matter systems [20–22] was used to explore the light-matter coupling of excitons in an extended MoSe<sub>2</sub>-WSe<sub>2</sub> heterostructure as a function of the cavity length at representative positions of HBLs selected by two-dimensional cavity imaging.

Before demonstrating cavity-control of excitons in a HBL system we identified the main signatures of intralayer and interlayer excitons with cryogenic photoluminescence (PL) spectroscopy. The crystal schematic of the van der Waals heterostructure, synthesized by overgrowth of ML MoSe<sub>2</sub> with a ML of WSe<sub>2</sub>, is shown in Fig. 1a. Upon optical excitation, photo-generated electrons and holes relax into the conduction band minima and valence band maxima of MoSe<sub>2</sub> and WSe<sub>2</sub> MLs, respectively [14]. After relaxation, zero-momentum excitons are formed by layer-separated electrons and holes of the same valley, while excitons with finite momentum emerge from Coulomb correlations among electrons and holes in dissimilar valleys. Even in the presence of inherent angular alignment, excitons in HBL stacks exhibit a large spread in their center-of-mass momenta just like twisted HBL systems [23]. This spread in momentum stems from Moiré superlattices [24] which in turn are a consequence of the lattice

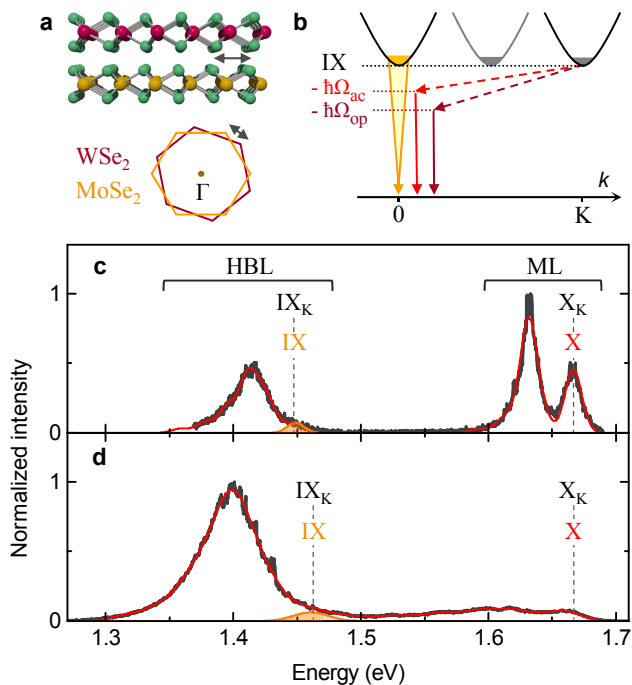


FIG. 1: **a**, Real space and reciprocal space schematics of a MoSe<sub>2</sub>-WSe<sub>2</sub> heterostructure with lattice mismatch symbolized by the arrow. **b**, Momentum-direct excitons (orange-shaded population) within the light cone decay radiatively with interlayer exciton PL energy IX. Momentum-dark excitons (grey-shaded populations away from the zero-momentum origin) decay only with the assistance of phonons and thus contribute to PL as acoustic and optical phonon sidebands downshifted from IX by  $\hbar\Omega_{ac}$  and  $\hbar\Omega_{op}$ , respectively. **c**, Spectral decomposition (red solid line) of the cryogenic PL from an as-grown MoSe<sub>2</sub>-WSe<sub>2</sub> sample into the contributions of radiative intralayer and interlayer excitons at energy X = 1.67 eV and IX = 1.45 eV, respectively, and phonon sidebands of momentum-dark intralayer and interlayer excitons (with energies X<sub>K</sub> and IX<sub>K</sub> resonant with X and IX, respectively, as indicated by the dashed lines). The zero phonon line of momentum-bright interlayer excitons is explicitly shown by the orange-shaded Gaussian with an inhomogeneous linewidth of  $\gamma = 16$  meV obtained from best-fit. **d**, Same but for a MoSe<sub>2</sub>-WSe<sub>2</sub> heterostructure on the cavity mirror. Best-fit energies of the intralayer and interlayer exciton energies (shown by the dashed lines) were X = 1.66 eV and IX = 1.46 eV, respectively, with with an inhomogeneous linewidth of  $\gamma = 32$  meV consistent with higher disorder than in the as-grown sample of **c**.

mismatch (symbolized by the arrows in Fig. 1a) in HBL systems built from dissimilar ML crystals. Thus, only the small fraction of zero-momentum interlayer excitons (labelled as IX in Fig. 1b) decays within the radiative lifetime of a few ns [14]. On the same timescale, a significant population of much longer lived excitons with center-of-mass momentum beyond the light cone (with exciton dispersions in Fig. 1b shifted away from the origin up to the maximum in-plane momentum K) will accumulate due to highly suppressed radiative decay.

In confocal PL spectroscopy, diffraction-limited excitation and detection spots sample a large number of Moiré superlattice cells and thus probe both momentum-bright and

momentum-dark interlayer excitons. The former emit PL directly at their bare energy of zero-momentum interlayer excitons IX. The latter, on the other hand, contribute to the PL spectrum as phonon sidebands [25, 26] downshifted from IX by the energy of acoustic or optical phonons ( $\hbar\Omega_{ac}$  or  $\hbar\Omega_{op}$ ) that compensate for momentum-mismatch in the light-matter coupling and thus enable radiative decay of momentum-dark excitons. Both the zero phonon line (ZPL) of momentum-bright excitons IX and the phonon sidebands of momentum-dark excitons IX<sub>K</sub> contribute to the intense red-most peak around 1.4 eV in the PL spectra of our as-grown and mirror-transferred MoSe<sub>2</sub>-WSe<sub>2</sub> HBLs shown in Fig. 1c and d, respectively. In addition to this low-energy HBL peak arising from interlayer excitons as in exfoliation-stacked heterostructures [14–17], intralayer MoSe<sub>2</sub> excitons contribute a pair of blue peaks to the PL around 1.65 eV [14]. Commonly, the upper and lower ML peaks are assigned to neutral and charged excitons (trions) in MoSe<sub>2</sub> [27], respectively.

In the presence of a long-lived reservoir of momentum-dark counterparts (X<sub>K</sub>) of momentum-bright neutral ML excitons (X), however, this assignment is ambiguous. In fact, the trion signatures as well as the extended red tail in the PL below X can be explained on the basis of phonon replicas of momentum-dark excitons alone [25]. We used this notion to decompose the PL spectra of Fig. 1c and d into contributions from momentum-bright and -dark intralayer (X and X<sub>K</sub>) and interlayer (IX and IX<sub>K</sub>) excitons with the energy positions of their respective ZPL identified from best-fit (red solid lines) and indicated by the dashed lines in Fig. 1c and d. The states X and X<sub>K</sub> as well as IX and IX<sub>K</sub> were assumed energy-degenerate by neglecting electron-hole exchange and modelled by Gaussian ZPLs with identical inhomogeneous linewidth  $\gamma$ . The differences in the absolute energies of X and IX as well as the difference in spectral broadening in the two samples probably stem from different dielectric environments, strain and other disorder. More remarkably, our spectral decomposition analysis, analogous to recent studies of complementary TMD systems [25, 26], not only explains the PL between X and IX in terms of higher-order phonon replicas activated by disorder [25], it also implies that only a small fraction of the characteristic HBL peak actually stems from radiative interlayer excitons IX (with ZPLs given explicitly by the yellow-shaded Gaussians in Fig. 1c and d). The predominant part of the HBL peak is ascribed to acoustic and optical phonon sidebands of the momentum-dark exciton reservoir at IX<sub>K</sub>.

In order to substantiate this new perspective on the PL signatures of HBLs we carried out time-resolved PL experiments on a mirror-transferred MoSe<sub>2</sub>-WSe<sub>2</sub> flake. Previous cryogenic studies of exfoliation-stacked MoSe<sub>2</sub>-WSe<sub>2</sub> heterostructures reported a broad range of phenomena for the dynamics of interlayer exciton PL with lifetimes in the range of 1 – 100 ns extracted from single- or multi-exponential decay fits [10, 14–17]. The broad-band interlayer HBL peak of our CVD-grown samples exhibits similar decay characteristics. The best approximation to the total HBL peak was ob-

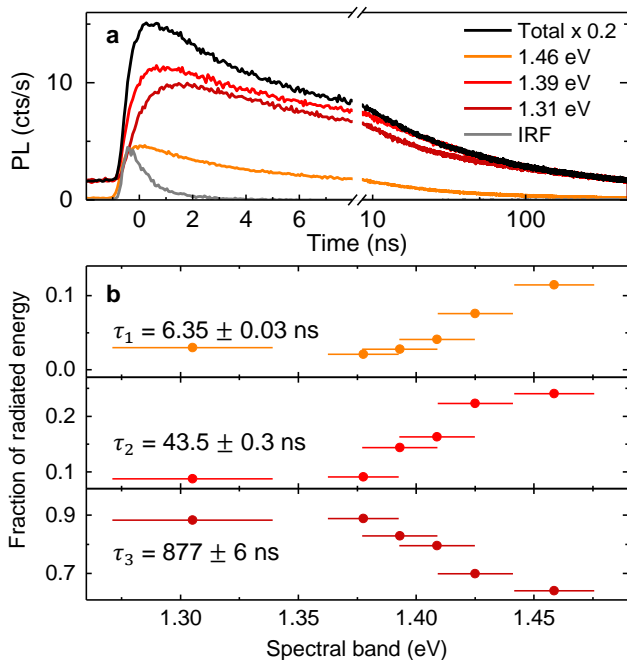


FIG. 2: **a**, PL decay measured in different spectral bands on a mirror-transferred  $\text{MoSe}_2$ - $\text{WSe}_2$  flake with the spectrum in Fig. 1d. Decay traces are shown in different colors for three spectral bands centered at 1.46, 1.39 and 1.31 eV together with the total decay trace in black (scaled by  $\times 0.2$ ) and the instrument response function (IRF) in grey. The decay of the total spectrally unfiltered PL was approximated best by three exponential decay channels with constants of 6, 43 and 877 ns. **b**, Relative contributions of the three decay channels to the total PL radiated into the spectral windows with central energies and widths represented by dots and bars, respectively. For each spectral window, the contributions were extracted from triple-exponential fits with decay constants fixed to the characteristic timescales of the total PL.

tained with three exponential decay channels characterized by lifetimes of  $\sim 6$ , 44 and 877 ns (see Supplementary Information for details). Interestingly, the contributions of the individual decay channels to the total radiated PL energy varied significantly across the HBL peak. By performing PL decay measurements in narrow spectral windows centered at variable energies as in Fig. 2a, we found that the relative weight of the slowest decay component with 877 ns decay constant increased at the expense of the more rapid components with 6 and 44 ns lifetimes as the spectral band of the measurement window was shifted to lower energies (Fig. 2b). In the red-most wing, interlayer PL was significantly delayed (note the prolonged rise-time of the PL traces in Fig. 2a recorded in the red wing) and nearly entirely dominated by the longest decay constant. Its finite value on the blue side of the peak is attributed to disorder-mediated slow multi-phonon decay channels [28] of intralayer excitons X.

The cross-over from short to long PL lifetimes upon progressive red-shift is consistent with our interpretation of the total HBL PL. Our model predicts a decrease for the PL contribution of the momentum-bright exciton state IX upon in-

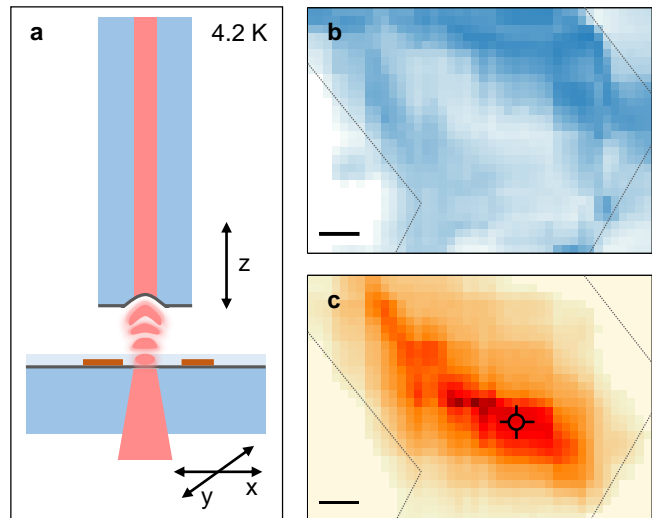


FIG. 3: **a**, Cavity setup at 4.2 K: the fiber-based micro-mirror forms the cavity together with a planar macro-mirror with CVD-grown  $\text{MoSe}_2$ - $\text{WSe}_2$  on top. Independent translational degrees of freedom enable lateral sample displacement and cavity length detuning. **b**, Transmission map recorded through the cavity with laser excitation at 635 nm (blue color corresponds to reduced transmission due to local variations in absorption and scattering). **c**, Map of integrated PL intensity recorded simultaneously with the transmission map (dark red color represents maximum intensity). The cross indicates the position on the flake used in the measurements of Fig. 2 and Fig. 4, the grey dashed lines indicate the boundaries of the flake. The scale bar is  $10 \mu\text{m}$  in both maps.

creasing red-shift from its ZPL, and this trend is consistently supported by the data in the upper panel of Fig. 2b. The secondary lifetime due to decay processes of momentum-dark interlayer excitons  $\text{IX}_K$  assisted by first-order acoustic and optical phonons exhibits the same trend yet at larger red-shifts (data in the central panel of Fig. 2b). Finally, the contribution of the third decay component stemming from higher-order decay processes assisted by multiple phonons is suppressed at small red-shifts and dominates only for largest red-shifts (data in the lower panel of Fig. 2b). Before proceeding we note that this framework of three characteristic decay components might be too rudimentary to capture the actual population dynamics of interlayer excitons in HBLs with a variety of decay channels associated with the spread in the exciton momenta by the Moiré effects and additional disorder (as evidenced by the PL in between X and IX peaks in Fig. 1d). However, it is also not obvious how to introduce three specific decay timescales in the framework of disorder-localized excitons commonly employed to motivate long-lived PL decays.

Bearing this limitation in mind we proceed by presenting results on cavity-control of the three characteristic PL decay channels. To this end, we complemented the macroscopic mirror with CVD-grown  $\text{MoSe}_2$ - $\text{WSe}_2$  flakes on top by a fiber micro-mirror in a cryogenic setup (see Supplementary Information for details). In brief, our optical Fabry-Pérot resonator, immersed in a helium bath cryostat at 4.2 K, is

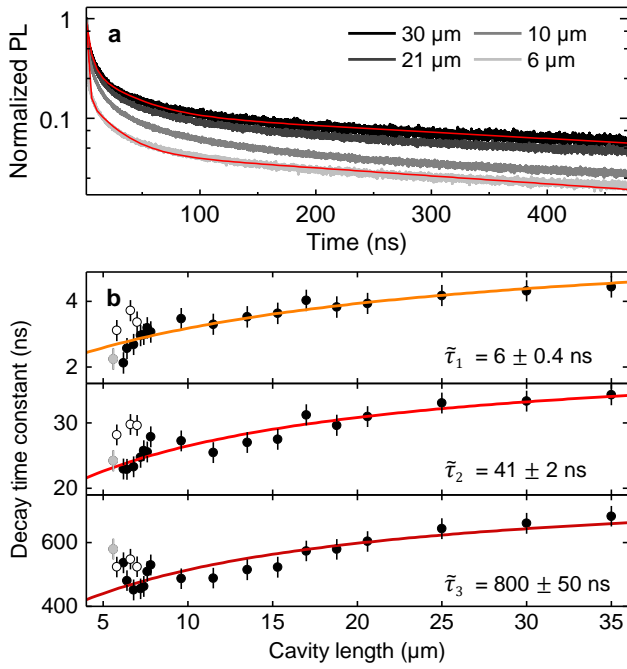


FIG. 4: **a**, Traces of interlayer exciton PL decay shown for four selected cavity lengths. The solid lines are fits to the data with three exponential decay constants. Note the speed up in the decay upon the reduction of the cavity length. **b**, Evolution of the characteristic decay constants with the cavity length. The solid lines show model fits according to the theory of generalized Purcell enhancement. Open circles represent data where the cavity mode was spectrally detuned from the resonance with the interlayer peak; data shown in light grey were discarded from the fit procedure due to presumable physical contact between the fiber and the mirror.

based on a single-mode fiber with a laser-machined concave end facet coated with silver and a protecting layer of  $\text{SiO}_2$ . The schematic drawing of the cavity setup with independent translational degrees of freedom along all three dimensions is shown in Fig. 3a. Lateral displacement of the sample mirror enabled coarse-tuning of the cavity length as well as two-dimensional positioning and profiling of the sample. The respective transmission and PL maps of the flake with PL data in Fig. 1d and Fig. 2 are shown in Fig. 3b and c.

The transmission of the excitation laser at 635 nm provided quantitative access to absorption and scattering inside the cavity. Sizeable ML absorption in the range of several percent [29] facilitated the detection of individual MLs and HBL via the cavity transmission. Scattering contrast at structural defects such as edges or transfer-related cracks provided additional guides to the identification of individual flakes. Equipped with the combined scanning capabilities and the information from transmission, it was straight forward to position the cavity into any point of interest of a given HBL flake. In addition, by recording PL spectra at each raster scan-point of the cavity simultaneously with the transmission, PL intensity maps were obtained within any spectral band of interest as shown for the interlayer exciton PL peak in Fig. 3c.

By monitoring both transmission and PL, we positioned the cavity on the spot indicated by the cross in Fig. 3c where data of Fig. 1d and Fig. 2 were recorded with confocal spectroscopy and performed PL decay measurements as a function of the cavity length. The respective decay traces of the HBL peak in the spectrum of Fig. 1d are shown in Fig. 4a for cavity lengths of 30, 21, 10 and 6  $\mu\text{m}$ . Clearly, the PL decay speeds up with decreasing cavity length. For a more quantitative analysis, the PL traces recorded at different cavity lengths were modeled by a convolution of the instrument response function (IRF) and a three-exponential decay with amplitudes and time constants of each decay channel as free fit parameters (see Supplementary Information for details). The corresponding model fits, shown as red solid lines in Fig. 4a, were used to extract the evolution of the short, intermediate and long decay time components with the cavity length.

The respective data, shown in Fig. 4b, clearly demonstrate cavity-control of all three characteristic decay channels. The lifetimes decrease with decreasing cavity length - a hallmark of Purcell enhancement which can be quantified by the ratio of the total decay rate in the cavity system  $\gamma_c$  to the free-space decay rate  $\gamma_{fs}$  as  $\gamma_c/\gamma_{fs} = 1 + C$ , where  $C$  is the Purcell factor. An estimate for the cavity-mediated Purcell enhancement can be obtained by identifying the values from confocal decay measurements with free-space lifetimes. Taking the smallest lifetime values for each decay channel from the data of Fig. 4b, this yields maximum measured Purcell factors of  $1.8 \pm 0.3$ ,  $0.8 \pm 0.1$  and  $0.9 \pm 0.1$  for the short, intermediate and long lifetime components, respectively. The difference in the Purcell factors highlights the different nature of the coupling between the corresponding decay channels and the cavity field, with interlayer momentum-bright excitons IX exhibiting higher coupling efficiency than phonon-mediated decay channels of momentum-dark excitons IX<sub>K</sub>.

The three different channels also exhibit pronounced differences in their response to cavity length detuning shown in Fig. 4b. At a cavity length of 35  $\mu\text{m}$ , several cavity modes are resonant with the HBL emission peak thus enhancing all possible emission channels simultaneously. For cavity lengths smaller than 9  $\mu\text{m}$ , however, the free spectral range of the cavity exceeded the linewidth of the HBL emission peak, rendering light-matter coupling sensitive to the spectral resonance condition. Open circles in Fig. 4b show the results for the off-resonance configurations in accord with cavity-inhibited radiative decay. In contrast, the on-resonance data (measured with a dense spacing of data points for  $\sim 6 - 8 \mu\text{m}$  cavity lengths in Fig. 4b) reflect the effect of cavity-enhancement with anti-correlated trends for short and long decay components at smallest cavity lengths consistent with spectrally distinct channels. At a nominal separation of  $\sim 5 \mu\text{m}$  (grey circles), physical contact between the fiber and the extended mirror was presumably reached, preventing further reduction of the cavity mode volume.

The data points recorded in contact of the fiber and the macro-mirror as well as all off-resonance data were discarded from the following analysis of the cavity-induced Purcell en-

hancement in the presence of pure dephasing [30]. On resonance, the generalized Purcell factor is  $C = (4g^2/\gamma_{fs})/(\kappa + \gamma_{fs} + \gamma_d)$ , where  $g$  is the coupling rate of the emitter to the cavity,  $\kappa$  is the cavity decay rate, and  $\gamma_d$  is the dephasing rate of the emitter. Both  $g$  and  $\kappa$  vary as a function of the cavity length [31–33]. By taking the inhomogeneous linewidth  $\gamma = 32$  meV obtained from model fits of Fig. 1d as an upper bound to the dephasing rate in our system (i. e. using  $\gamma_d = \gamma$ ), we fitted each data set of Fig. 4b according to the model for the generalized Purcell enhancement (see Supplementary Information for details). The resulting best fits, shown as solid lines in Fig. 4b, were obtained with free-space lifetimes of  $6.2 \pm 0.4$ ,  $41 \pm 2$  and  $800 \pm 50$  ns for the three sets of data in the respective panels of Fig. 4b. These asymptotic values at infinite cavity length extracted from the model fit agree well with the decay times determined in confocal PL spectroscopy (data in Fig. 2b).

With this strong confidence in the correspondence between the free-space lifetime values extracted from the model of generalized Purcell enhancement and the decay times obtained in the absence of the cavity with confocal PL spectroscopy, the model allows now to extrapolate maximum Purcell enhancement  $C^{\max}$  that can be achieved at the peak wavelength of the HBL emission  $\lambda$  for a mirror separation of  $\lambda/2$ . The model yields  $C^{\max}$  of  $2.5 \pm 0.2$  for the short and  $1.4 \pm 0.1$  for both the intermediate and long lifetime channels, respectively. For the same limit of the intermirror spacing of  $\lambda/2$  and a cavity volume of  $\sim \lambda^3$ , the model also quantifies the light-matter coupling strength  $g$  as  $170 \pm 8$ ,  $50 \pm 2$  and  $11 \pm 0.7$   $\mu\text{eV}$  for the short, intermediate and long decay channel, respectively. These values are rather robust against variations in the dephasing rate, with  $g$  changing by less than 25 % for  $\gamma_d$  in the range of 10 – 70 meV. At the same time light-matter coupling was sensitive to material and environmental characteristics with up to 50 % changes in  $g$  and about 30 % variations in the free-space PL lifetimes on different positions of the same flake and different flakes.

The values for the light-matter coupling strength  $g$  of interlayer excitons in our CVD-grown  $\text{MoSe}_2\text{-WSe}_2$  HBL sample are two to three orders of magnitude smaller than the coupling rates reported for MLs TMDs [5–8]. This striking difference in light-matter coupling, fully consistent with the spatially indirect nature of momentum-bright and momentum dark interlayer excitons in HBL systems, yields tight constraints on the observation of interlayer exciton-polariton phenomena in the strong-coupling regime of HBL – cavity hybrids. To ensure  $g > \kappa + \gamma_d$  for strong-coupling, cavities with higher quality factors are readily available [20], yet much improved HBL crystals and environmental conditions will be required to reduce dephasing. However, in view of radiatively limited linewidths achieved for ML TMDs by encapsulation with hexagonal boron nitride [34–36], further progress towards the realization of dipolar exciton-polariton gases in cavity – van der Waals heterostructure systems seems feasible.

**Acknowledgments:** We thank Guillaume Cassabois (Université Montpellier) for fruitful discussions and acknowledge

support from Yongji Gong (Beihang University) and Pulickel M. Ajayan (Rice University) on material growth parameters at the initial stage of project. This research was funded by the European Research Council under the ERC Grant Agreement no. 336749, the Volkswagen Foundation, and the German Excellence Initiative via the Nanosystems Initiative Munich (NIM). A. H. also acknowledges support from the Center for NanoScience (CeNS) and LMUinnovativ. A. D. M. acknowledges support from LDRD program and CINT at LANL.

- 
- [1] A. Splendiani, L. Sun, Y. Zhang, T. Li, J. Kim, C.-Y. Chim, G. Galli, and F. Wang, *Nano Lett.* **10**, 1271 (2010).
  - [2] K. F. Mak, C. Lee, J. Hone, J. Shan, and T. F. Heinz, *Phys. Rev. Lett.* **105**, 136805 (2010).
  - [3] D. Xiao, G.-B. Liu, W. Feng, X. Xu, and W. Yao, *Phys. Rev. Lett.* **108**, 196802 (2012).
  - [4] X. Xu, W. Yao, D. Xiao, and T. F. Heinz, *Nat. Phys.* **10**, 343 (2014).
  - [5] X. Liu, T. Galfsky, Z. Sun, F. Xia, E.-c. Lin, Y.-H. Lee, S. Kena-Cohen, and V. M. Menon, *Nature Photonics* **9**, 30 (2015).
  - [6] L. C. Flatten, Z. He, D. M. Coles, A. A. P. Trichet, A. W. Powell, R. A. Taylor, J. H. Warner, and J. M. Smith, *Sci. Rep.* **6** (2016).
  - [7] N. Lundt, A. Marynski, E. Cherotchenko, A. Pant, X. Fan, G. Sek, S. Tongay, A. V. Kavokin, S. Höfling, and C. Schneider, *arXiv:1603.05562* (2016).
  - [8] N. Lundt, P. Nagler, A. Nalitov, S. Klemmt, M. Wurdack, S. Stoll, T. H. Harder, S. Betzold, V. Baumann, A. V. Kavokin, et al., *2D Mater.* **4**, 025096 (2017).
  - [9] M. Sidler, P. Back, O. Cotlet, A. Srivastava, T. Fink, M. Kroner, E. Demler, and A. Imamoglu, *Nat. Phys.* **13**, 255 (2017).
  - [10] P. Rivera, K. L. Seyler, H. Yu, J. R. Schaibley, J. Yan, D. G. Mandrus, W. Yao, and X. Xu, *Science* **351**, 688 (2016).
  - [11] M. M. Fogler, L. V. Butov, and K. S. Novoselov, *Nat. Commun.* **5**, 4555 (2014).
  - [12] J. Kang, S. Tongay, J. Zhou, J. Li, and J. Wu, *Appl. Phys. Lett.* **102**, 012111 (2013).
  - [13] M.-H. Chiu, C. Zhang, H.-W. Shiu, C.-P. Chuu, C.-H. Chen, C.-Y. S. Chang, C.-H. Chen, M.-Y. Chou, C.-K. Shih, and L.-J. Li, *Nat. Commun.* **6**, 7666 (2015).
  - [14] P. Rivera, S. John R., A. M. Jones, J. S. Ross, S. Wu, G. Aivazian, P. Klement, K. Seyler, G. Clark, N. J. Ghimire, et al., *Nat. Commun.* **6**, 6242 (2015).
  - [15] B. Müller, A. Steinhoff, B. Pano, F. Jahnke, A. Holleitner, and U. Wurstbauer, *arXiv:1703.09566* (2017).
  - [16] C. Jiang, W. Xu, A. Rasmitha, Z. Huang, K. Li, Q. Xiong, and W.-b. Gao, *arXiv:1703.03133* (2017).
  - [17] P. Nagler, G. Plechinger, M. Ballotin, A. Mitioglu, S. Meier, N. Paradiso, C. Strunk, A. Chernikov, P. Christianen, C. Schüller, et al., *2D Mater.* (2017).
  - [18] Y. Gong, J. Lin, X. Wang, G. Shi, S. Lei, Z. Lin, X. Zou, G. Ye, R. Vajtai, B. I. Yakobson, et al., *Nat. Mater.* **13**, 1135 (2014).
  - [19] M.-Y. Li, Y. Shi, C.-C. Cheng, L.-S. Lu, Y.-C. Lin, H.-L. Tang, M.-L. Tsai, C.-W. Chu, K.-H. Wei, J.-H. He, et al., *Science* **349**, 524 (2015).
  - [20] T. Hümmer, J. Noe, M. S. Hofmann, T. W. Hänsch, A. Högele, and D. Hunger, *Nat. Commun.* **7**, 12155 (2016).
  - [21] H. Kaupp, T. Hümmer, M. Mader, B. Schleder, J. Benedikter, P. Haeusser, H.-C. Chang, H. Fedder, T. W. Hänsch, and

- D. Hunger, Phys. Rev. Applied **6**, 054010 (2016).
- [22] J. Benedikter, H. Kaupp, T. Hümmer, Y. Liang, A. Bommer, C. Becher, A. Krueger, J. M. Smith, T. W. Hänsch, and D. Hunger, Phys. Rev. Applied **7**, 024031 (2017).
- [23] H. Yu, Y. Wang, Q. Tong, X. Xu, and W. Yao, Phys. Rev. Lett. **115**, 187002 (2015).
- [24] Q. Tong, H. Yu, Q. Zhu, Y. Wang, X. Xu, and W. Yao, Nat. Phys. **13**, 356 (2016).
- [25] J. Lindlau, C. Robert, V. Funk, M. Förg, L. Colombier, A. Neumann, T. Taniguchi, K. Watanabe, M. M. Glazov, X. Marie, et al., arXiv:1710.00988 (2017).
- [26] J. Lindlau, M. Selig, A. Neumann, L. and Colombier, J. Kim, G. Berghäuser, F. Wang, E. Malic, and A. Högele, arXiv:1710.00989 (2017).
- [27] J. S. Ross, S. Wu, H. Yu, N. J. Ghimire, A. M. Jones, G. Aivazian, J. Yan, D. G. Mandrus, D. Xiao, W. Yao, et al., Nat. Commun. **4**, 1474 (2013).
- [28] G. Cassaboïs, P. Valvin, and B. Gil, Phys. Rev. B **93**, 035207 (2016).
- [29] Y. Li, A. Chernikov, X. Zhang, A. Rigosi, H. M. Hill, A. M. van der Zande, D. A. Chenet, E.-M. Shih, J. Hone, and T. F. Heinz, Phys. Rev. B **90**, 205422 (2014).
- [30] A. Auffeves, D. Gerace, J.-M. Gérard, M. F. Santos, L. C. Andreani, and J.-P. Poizat, Phys. Rev. B **81** (2010).
- [31] V. Savona, L. C. Andreani, P. Schwendimann, and A. Quattropani, Solid State Commun. **93**, 733 (1995).
- [32] B. Besga, C. Vaneph, J. Reichel, J. Estève, A. Reinhard, J. Miguel-Sánchez, A. Imamoğlu, and T. Volz, Phys. Rev. Applied **3**, 014008 (2015).
- [33] D. Hunger, T. Steinmetz, Y. Colombe, C. Deutsch, T. W. Hänsch, and J. Reichel, New J. Phys. **12**, 065038 (2010).
- [34] G. Wang, C. Robert, M. M. Glazov, F. Cadiz, E. Courtade, T. Amand, D. Lagarde, T. Taniguchi, K. Watanabe, B. Urbaszek, et al., Phys. Rev. Lett. **119**, 047401 (2017).
- [35] F. Cadiz, E. Courtade, C. Robert, G. Wang, Y. Shen, H. Cai, T. Taniguchi, K. Watanabe, H. Carrere, D. Lagarde, et al., Phys. Rev. X **7**, 021026 (2017).
- [36] O. A. Ajayi, J. V. Ardelean, G. D. Shepard, J. Wang, A. Antony, T. Taniguchi, K. Watanabe, T. F. Heinz, S. Strauf, X.-Y. Zhu, et al., arXiv:1702.05857 (2017).

## SUPPLEMENTARY INFORMATION

### Experimental methods

#### *Chemical vapor deposition of TMD heterobilayers*

First, MoSe<sub>2</sub> ML was grown by selenization of molybdenum trioxide (MoO<sub>3</sub>) powder. SiO<sub>2</sub>/Si substrate along with MoO<sub>3</sub> powder boat were placed at the center of a chemical vapor deposition (CVD) furnace, which was heated to 750 °C in 15 min and held for 20 min. SiO<sub>2</sub>/Si substrate was facing down in close proximity with MoO<sub>3</sub> powder. Selenium (Se) powder vaporized at 200 °C was used as Se source, and a mixture of argon and hydrogen (15% hydrogen) at 50 SCCM was used as the carrier gas. The as-grown MoSe<sub>2</sub>/SiO<sub>2</sub>/Si was then transferred to a separate CVD setup for subsequent WSe<sub>2</sub> growth similar to the growth method of MoSe<sub>2</sub>. Specifically, selenization of tungsten oxide (WO<sub>3</sub>) was per-

formed at 900 °C in the presence of 100 SCCM carrier gas. WSe<sub>2</sub> would grow on top of MoSe<sub>2</sub> from its edges, creating MoSe<sub>2</sub>/WSe<sub>2</sub> vertical heterostructures. No additional treatment was necessary prior to WSe<sub>2</sub> growth due to thermal removal of possible physisorbed molecule gases on MoSe<sub>2</sub> during the transfer in air. As-grown heterostructures were studied in spectroscopy or transferred onto a mirror using established polymer-supported wet method. To this end poly(methyl methacrylate) (PMMA) was spin-coated on the heterostructure and lifted off in 1M potassium hydroxide (KOH) in water. Finally, the PMMA-supported film with MoSe<sub>2</sub>-WSe<sub>2</sub> vertical heterostructures on the mirror was rinsed in three cycles of water at room temperature to remove possible KOH residue.

#### *Photoluminescence microscopy and spectroscopy*

Photoluminescence experiments were performed in a home-built cryogenic scanning cavity setup. The sample was mounted on piezo-stepping units (attocube systems ANPxy101 and ANPz102) for positioning with respect to the cavity mode. The cavity unit was placed in a dewar with an inert helium atmosphere at a pressure of 20 mbar and immersed in liquid helium at 4.2 K. Excitation around 635 – 705 nm was performed with a wavelength-tunable white light laser system (NKT SuperK Extreme and SuperK Varia) with repetition rates down to 2 MHz. The PL was either spectrally dispersed by a monochromator (Princeton Instruments Acton SP 2500) and recorded with a nitrogen-cooled silicon CCD (Princeton Instruments PyLoN) or detected with avalanche photodiodes (Excelitas SPCM-AQRH or PicoQuant  $\tau$ SPAD).

#### *Scanning cavity microscopy*

The cavity was composed of a fiber micro-mirror and a macroscopic mirror with MoSe<sub>2</sub>-WSe<sub>2</sub> vertical HBL on top. The macro-mirror was coated with  $\sim$  30 nm of silver and a spacer layer of SiO<sub>2</sub> with thickness designed to place the HBL at a field antinode. The effective radius of curvature of the central depression in the laser-machined fiber end facet was 136  $\mu$ m. The facet was coated with  $\sim$  50 nm silver and a protection layer of SiO<sub>2</sub>. Three translational degrees of freedom of the sample on the mirror was enabled by cryogenic piezo-stepping units (attocube systems ANPxy101 and ANPz102) to provide both lateral scans and coarse-tuning of the cavity length. Cavity fine-tuning was achieved by displacing the fiber-mirror with an additional piezo. Excitation by a diode laser at 635 nm was provided via the optical fiber and both transmission and PL were detected through the planar macro-mirror with the heterostructure on top. Two-dimensional scans were performed with a cavity length of  $\sim$  22  $\mu$ m resulting in a mode-waist of 3.2  $\mu$ m for the excitation laser and a mode-waist of 3.7  $\mu$ m for the detected PL around 880 nm.

## Analysis of time-correlated photoluminescence decay

### Deconvolution procedure

Time-correlated photoluminescence (TCPL) decay traces recorded with two different avalanche photodiodes (APDs) used in confocal spectroscopy and cavity setups with 900 and 440 ps response times, respectively, were modeled as a convolution of the APD instrument response function (IRF) with multi-exponential decay functions as follows:

$$I(t) = I_0 + A_0 \cdot e^{-2 \cdot [(t-t_0)/w]^2} + \sum_{k=1}^N A_k \cdot e^{(-t/\tau_k)}, \quad (1)$$

where the first term  $I_0$  quantifies the APD dark counts, the second term is the APD IRF approximated by a Gaussian with the temporal resolution  $w$ , and the third is the sum of  $N$  individual exponential decay channels  $k$  with amplitude  $A_k$  and characteristic decay time  $\tau_k$ . The dark counts and the response times  $w$  of both APDs were calibrated experimentally as in Fig. 1. The time  $t_0$ , set to the maximum of each TCPL trace, was an input parameter to the fits with the amplitudes  $A_k$  and the decay times  $\tau_k$  as free fit parameters. A representative model fit to a TCPL trace (recorded for a cavity length of 30  $\mu\text{m}$ ) obtained with three decay channels is shown in Fig. 1.

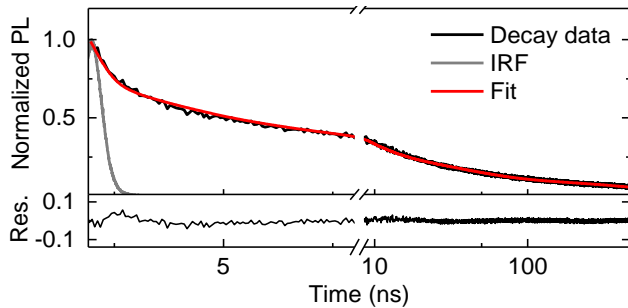


Figure S1: Upper panel: Normalized time-correlated PL decay at a cavity length of 30  $\mu\text{m}$  (black), experimental APD instrument response function (grey), and model fit with three exponential decay channels (red solid line with  $\tau_1 = 4.3$  ns,  $\tau_2 = 33$  ns,  $\tau_3 = 660$  ns). Lower panel: Residuum of the fit.

### Determining the minimum number of decay channels

To identify the minimum number of channels required to describe the multi-exponential decay characteristics of the HBL emission, the TCPL traces of the cavity measurements were fitted with a varying number of channels using Eq. 1. The number of possible channels was increased from two up to five. For each number this analysis was applied to the whole set of TCPL measurements from 35  $\mu\text{m}$  down to 5  $\mu\text{m}$  cavity length. The quality of each fitting procedure was extracted by calculating the  $\chi^2$ -value. An average  $\chi^2$ -value for all analyzed cavity lengths is shown in Fig. 2a. For an increasing

number of possible channels the  $\chi^2$ -value decreases down to the measurement noise level.

Analyzing the  $\chi^2$ -value restricts the analysis to the quantity of the overlap of the best-fit function with the measured data, neglecting the possible errors of the individual free fit parameters. According to Equation 1 each fitting procedure has a whole set of free fit parameters with characteristic errors. For an adequate description of the TCPL data these errors should be minimized. Therefore, an averaged error was calculated for each fit using the errors of the individual free fit parameters. A mean value for all corresponding lifetime traces results in an overall error of the free fit parameters,  $\delta_N$ . The corresponding errors are shown in Fig. 2b. The more possible decay channels contribute, the higher is the overall error  $\delta_N$  of the free fit parameters.

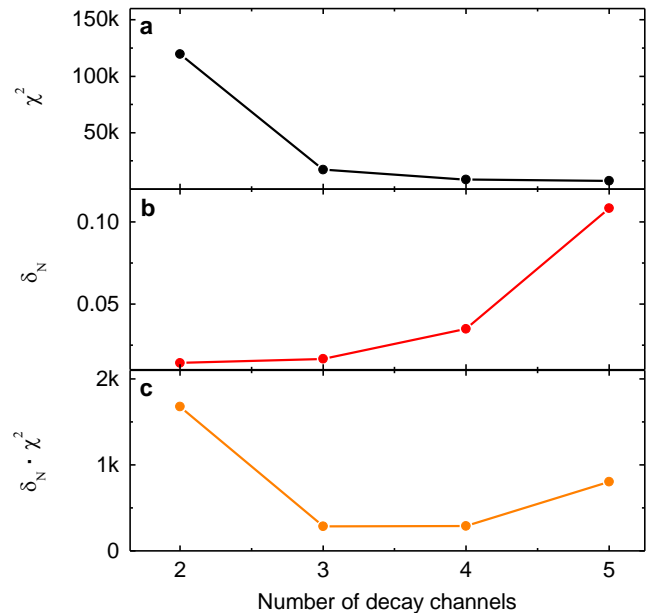


Figure S2: **a**, Best-fit  $\chi^2$  average, obtained by averaging  $\chi^2$  values of multi-channel best-fits for all measurements at variable cavity lengths, as a function of the number of decay channels. **b**, Averaged and normalized parameter errors  $\delta_N$  for the corresponding data. **c**, Product  $\delta_N \cdot \chi^2$  of both error types. The minimum of the product at  $N = 3$  indicates that three decay channels are best suited to approximate the multi-channel decay characteristics of the HBL peak in Fig. 1 of the main text.

In order to have a quantity that respects both error-types, the product  $\delta_N \cdot \chi^2$  was calculated. The result is shown in Fig. 2c. This product has its minimum for three decay channels, indicating that this description is best suited to approximate the HBL emission for analysis of both confocal and cavity TCPL data.

### Cavity-emitter coupling

The general dependence of the cavity decay rate  $\kappa$  and the coupling rate  $g$  on the cavity length  $L$  is given in the framework of a coupled quantum well to a two dimensional cavity as [31]:

$$\kappa = 2 \cdot \frac{1 - \sqrt{R}}{\sqrt{R}} \frac{c}{n_c L_c}. \quad (2)$$

The cavity decay rate  $\kappa$  is extracted as the full-width at half-maximum linewidth of broadband transmission spectra recorded for an empty cavity (i.e. off MoSe<sub>2</sub>-WSe<sub>2</sub> flakes) at a given cavity length. The numbers of  $\kappa$  we extract are consistent with reflectivity values of  $R = 0.87$ , which allows to simplify Eq. 2 as:

$$\kappa(L) = \kappa_0 \cdot \frac{\lambda}{2L}, \quad (3)$$

where  $\kappa_0$  is the cavity decay rate at a mirror separation of  $\lambda/2$ . For our cavity system we obtain  $\kappa_0 = 410$  meV. Similar con-

siderations for the collective coupling rate  $g_k$  yield for each individual channel:

$$g_k(L) = g_{0,k} \cdot \sqrt{\frac{\lambda}{2L}}. \quad (4)$$

In the next step we use  $\gamma_c/\gamma_{fs} = 1 + C$ , the ratio of the total decay rate in the cavity system  $\gamma_c$  to the free-space decay rate  $\gamma_{fs}$ , together with the expression for the generalized Purcell factor  $C = (4g^2/\gamma_{fs})/(\kappa + \gamma_{fs} + \gamma_d)$  [30] to obtain the equation for the individual decay channels:

$$\gamma_{c,k} = \gamma_{fs,k} \cdot \left( 1 + \frac{4g_k^2/\gamma_{fs,k}}{\kappa + \gamma_{fs,k} + \gamma_d} \right),$$

with  $\gamma_d$  being the dephasing rate of the emitter. The functional dependence of the rate enhancement on the cavity length can be obtained by using Eq. 3 and 4. In a final step the rate enhancement is converted into a lifetime change via  $\tau_{c,k} = 1/\gamma_{c,k}$  and  $\tilde{\tau}_k = 1/\gamma_{fs,k}$ . The resulting fitting function takes  $g_{0,k}$  and  $\tilde{\tau}_k$  as free fitting parameters.